Weierstraß-Institut
für Angewandte Analysis und Stochastik
Leibniz-Institut im Forschungsverbund Berlin e. V.

Dynamics of micro-integrated external-cavity diode lasers: simulations, analysis and experiments

Mindaugas Radziunas[1], Vasile Z. Tronciu[2] , Erdenetsetseg Luvsandamdin[3],

Christian Kürbis[3], Andreas Wicht[3], Hans Wenzel[3]

submitted: July 10, 2014

[1] Weierstrass Institute
   Mohrenstr. 39
   10117 Berlin, Germany
   E-Mail: Mindaugas.Radziunas@wias-berlin.de

[2] Department of Physics
   Technical University of Moldova
   bd. Stefan cel Mare 168
   Chisinau MD-2004, Moldova
   E-Mail: tronciu@mail.utm.md

[3] Ferdinand-Braun-Institut, Leibniz-Institut für Höchstfrequenztechnik
   Gustav-Kirchhoff-Str. 4
   12489 Berlin, Germany
   E-Mail: erdenetsetseg.luvsandamdin@fbh-berlin.de
         christian.kuerbis@fbh-berlin.de
         andreas.wicht@fbh-berlin.de
         hans.wenzel@fbh-berlin.de

No. 1981

Berlin 2014

WI AS

Abstract

This paper reports the results of numerical and experimental investigations of the dynamics of an external cavity diode laser device composed of a semiconductor laser and a distant Bragg grating, which provides an optical feedback. Due to the influence of the feedback, this system can operate at different dynamic regimes. The traveling wave model is used for simulations and analysis of the nonlinear dynamics in the considered laser device. Based on this model, a detailed analysis of the optical modes is performed, and the stability of the stationary states is discussed. It is shown, that the results obtained from the simulation and analysis of the device are in good agreement with experimental findings.

1 Introduction

During recent years the control and stabilization of laser emission of semiconductor lasers (SLs) by an external cavity has received considerable attention. In particular, the integration of a Bragg grating into the laser cavity allows a stabilization of the emission wavelength as required by many applications such as frequency conversion, quantum-optical experiments and coherent optical communication [1, 2, 3]. Recently, a novel micro-integration approach was used to build a compact, narrow linewidth External Cavity Diode Laser (ECDL) with a volume holographic Bragg grating [4] ideally suited for quantum-optical experiments in space.

Semiconductor lasers subject to the delayed optical feedback from a distant mirror have been investigated extensively during the past two decades. Different dynamic regimes, including continuous-wave (cw) states, periodic and quasi-periodic pulsations, low frequency fluctuations, and a coherent collapse were examined (see Ref. [5] and references therein). A simplest method for modeling a semiconductor laser with a *weak* optical feedback is given by the Lang-Kobayashi (LK) model [6], which is the rate equation based system of delayed differential equations. Allthough it is relatively simple, the LK model admits a reasonable qualitative agreement with experiments and, therefore, provides a good understanding of nonlinear dynamics in the considered device [7]. The LK modeling approach was also successfully used to get a deep understanding of the stabilization or destabilization of the cw state by different configurations of the external cavity [8, 9].

On the other hand, the LK model is mostly suited for study of laser systems with small optical feedback and large ratio between the lengths of the external cavity and the laser, such that the length of the emitter itself can be neglected. A more appropriate way to describe the dynamics of semiconductor lasers with a *short* external cavity is given by the Traveling Wave (TW) model, which is a partial differential equation model that includes the spatial (longitudinal) distribution of the fields [10, 11]. This model is well suited not only for simulations of ECDL devices, but also for

a detailed study of coexisting stationary states [9] determined by longitudinal modes [12], and for numerical continuation and bifurcation analysis [13]. The TW model is used also in the present paper, which is devoted to an investigation of the dynamics of the ECDL device composed of an active semiconductor section and a distant BG that provides an optical feedback.

The paper is organized as follows. The device structure and mathematical model are described in Section 2. Section 3 introduces the concept of the mode analysis and discusses the stability of the cw states. Section 4 is devoted to comparison of experimental and theoretical results and a consecutive explanation of the experimental observations. A more detailed theoretical study of parameters and optimization of the ECDL are discussed in Section 5.

2   Setup and mathematical model

2.1   Laser setup

The micro-integrated ECDL studied in this paper and schematically shown in Fig. 1 consists of an active section (S_a), a long external volume holographic Bragg grating (BG, S_b), and a glass lens (S_l) closely located at the inner facet of the active section. Two air gaps $S_{g'}$ and $S_{g''}$ separate the active section from the lens and the lens from the BG, respectively. All parts are micro-integrated on an AlN ceramic base plate (micro-optical bench) with a footprint of only $25 \times 80\,\text{mm}^2$. The resonator is formed between the outer facet of the active section and the BG.
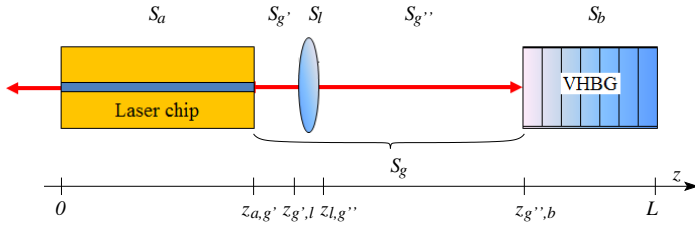

Figure 1: Schematic representation of the ECDL device.

The active section is a ridge-waveguide laser chip having a ridge width of $W = 4\,\mu$m similarly as described in [14]. The active zone consisting of a tensile-strained GaAsP double quantum well is embedded in an AlGaAs based super large optical cavity resulting in a vertical far-field divergence of only $12°$ (full width at half maximum). The laser emits a fundamental spatial mode transverse magnetic polarized.

2.2   Model equations

It is assumed, that the TW equations

$$\frac{n_g}{c_0}\partial_t E^\pm = \left[\mp\partial_z - i\beta(N, I)\right]E^\pm - i\kappa E^\mp + F_{sp}^\pm \qquad (1)$$

govern the dynamics of the slowly varying complex amplitudes $E^+(z, t)$ and $E^-(z, t)$ of the counter-propagating optical fields within each part of the laser. Here, c_0 is the speed of light in

2

vacuum, $F_{sp}^{\pm}$ is the stochastic spontaneous emission term in the active section S_a, n_g is the group index (different within different parts of the device), and κ is the field coupling coefficient (non-vanishing only in the Bragg grating S_b).

At the output ports of the ECDL ($z = 0$ and $z = L$) as well as at the interfaces $z = z_{k,j}$ of the adjacent parts S_k and S_j of the device where $k, j \in \{a, g', l, g'', b\}$ (see Fig. 1), the complex optical fields are related by the following reflection/transmission conditions [12]:

$$
\begin{aligned}
E^+(0,t) &= -r_0^* E^-(0,t), \qquad E^-(L,t) = r_L E^+(L,t), \\
E^+(z_{k,j}^+, t) &= -r_{k,j}^* E^-(z_{k,j}^+, t) + t_{k,j} E^+(z_{k,j}^-, t), \\
E^-(z_{k,j}^-, t) &= r_{k,j} E^+(z_{k,j}^-, t) + t_{k,j} E^-(z_{k,j}^+, t).
\end{aligned}
\tag{2}
$$

Here $z_{k,j}^-$ and $z_{k,j}^+$ denote the left and the right sides of the section interface, whereas $r_{k,j}$ are the complex field amplitude reflectivity coefficients ($|r_{k,j}| \leq 1$) and $t_{k,j} = \sqrt{1 - |r_{k,j}|^2}$ are the transmission coefficients.

The relative propagation factor β is given by

$$
\beta = \delta - i\frac{\alpha}{2} - i\frac{\mathcal{D}}{2} + \delta_T(I) + i\frac{(1 + i\alpha_H)\Gamma g'(N - N_{\mathrm{tr}})}{2}.
\tag{3}
$$

Outside the active section S_a the only non-vanishing terms in the expression (3) can be the internal loss constant α and the field phase tuning δ. In the absence of the field reflections at the edges of the lens ($r_{g',l} = r_{l,g''} = 0$) as it is considered in this paper, the three sequent parts $S_{g'}$, S_l, and $S_{g''}$ of the ECDL can be treated as a single *gap* section S_g with the averaged group index $\langle n_g \rangle_g$, phase tuning $\langle \delta \rangle_g$, and loss $\langle \alpha \rangle_g$. Here,

$$
\langle \zeta \rangle_k = \frac{1}{|S_k|} \int_{S_k} \zeta(z) dz
$$

denotes a spatial average of a function ζ over any ECDL section S_k, whereas $|S_k|$ is the length of S_k. The TW equations (1) in S_g can be easily resolved implying

$$
\begin{aligned}
E^+(z_{g'',b}^-, t) &= \sqrt{\eta} e^{i\varphi/2} E^+(z_{a,g'}^+, t - \tau_g), \\
E^-(z_{a,g'}^+, t) &= \sqrt{\eta} e^{i\varphi/2} E^-(z_{g'',b}^-, t - \tau_g),
\end{aligned}
$$

where

$$
\eta = e^{-\langle \alpha \rangle_g |S_g|}, \quad \frac{\varphi}{2} = -\langle \delta \rangle_g |S_g|, \quad \text{and} \quad \tau_k = \frac{\langle n_g \rangle_k |S_k|}{c_0}
$$

are the intensity attenuation, the phase shift of the forward or backward field during its propagation along S_g, and the field propagation time along each ECDL part S_k, respectively.

Within the active section S_a, the remaining terms of the propagation factor β are nontrivial. The operator $\mathcal{D}$ together with the induced polarization functions $P^{\pm}(z,t)$ are used to model the dispersion of material gain by a Lorentzian approximation [10]:

$$
\mathcal{D}E^{\pm} = \overline{g}(E^{\pm} - P^{\pm}), \qquad \partial_t P^{\pm} = \overline{\gamma}(E^{\pm} - P^{\pm}) + i\overline{\omega}P^{\pm},
\tag{4}
$$

3

where $\overline{g}$, $\overline{\omega}$, $2\overline{\gamma}$ are the amplitude, the relative central frequency, and the full width at the half maximum of this Lorentzian. The function $\delta_T(I)$ represents the dependence of the refractive index on the heating induced by the injected current I, e.g. [15]:

$$\delta_T(I) = c_T I. \tag{5}$$

Finally, β depends also on the carrier density dependent gain and index change functions determined by the confinement factor Γ, differential gain g', linewidth enhancement (Henry) factor α_H, and transparency carrier density N_{tr}. Due to the fact, that in the ECDL under study the overall variation of the carrier density N is small, a linear dependence on N has been assumed.

The longitudinal distribution of the local photon density $|E(z,t)|^2 = |E^+|^2 + |E^-|^2$ within the active section S_a of the ECDL deviates only slightly from its spatial average, $\langle|E|^2\rangle_a$. For this reason we neglect the spatial hole-burning of carriers and define the evolution of the spatially-uniform carrier density $N(t)$ in the active section S_a by the following rate equation:

$$\partial_t N = \frac{I}{q\sigma|S_a|} - \left(AN + BN^2 + CN^3\right) - \frac{c_0}{n_g}\Re\sum_{\nu=\pm}\langle E^{\nu*}\left[\Gamma g'(N-N_{\text{tr}}) - \mathcal{D}\right]E^\nu\rangle_a, \tag{6}$$

where A, B, C are carrier recombination parameters, I, σ, and q denote the injected current, the cross-section area of the active zone, and the electron charge. The emitted field power at the facet $z = 0$ is given by

$$P_{\text{o}}(t) = (1 - |r_0|^2)\frac{\sigma c_0}{n_g}\frac{hc_0}{\lambda_0}|E^-(0,t)|^2, \tag{7}$$

where h is the Planck constant, λ_0 is the central wavelength, and $1 - |r_0|^2$ is the field intensity transmission through the facet.

2.3 Typical parameters

The ECDL operates at $\lambda_0 = 0.78\mu$m. As it was mentioned above, the amplitude reflectivities $r_{g',l} = r_{l,g''} = 0$. Other reflectivities are $r_{a,g'} = 0.01$, $r_{g'',b} = r_L = 0$, and $r_0 = \sqrt{0.3}$. The lengths of sections are $|S_a| = 1$ mm, $|S_b| = 6$ mm, and $|S_g| = 30$ mm (where $|S_{g'}|$, $|S_l|$, and $|S_{g''}|$ are 1, 2, and 27 mm, respectively).

The numerical scheme used for integration of the TW equations (1) implies the condition $h_t = (n_g/c_0)h_{z,k}$ [12] on the temporal domain discretization step h_t and the spatial steps $h_{z,k}$ within each ECDL section S_k. All sections should consist of an integer number of steps h_z, i.e. $|S_k|n_g/(c_0 h_t)$ should be integer for all k. Since the group indices n_g in individual sections, in general, are different, one can fulfil this condition simultaneously for all S_k either by a careful choice of the section lengths, or by a corresponding adaptation of n_g. The group indices n_g in S_a, S_b, S_l, and $S_{g',g''}$ used in this paper are 4.1, 1.48625, 1.6005, and 1, respectively (such that $\langle n_g\rangle_g$ in S_g is, approximately, 1.04).

The numerical grid of the considered problem is determined by the temporal steps $h_t \approx 68.33$ fs, whereas the longitudinal domain $[0, L]$ of the whole ECDL is discretized by 2157 spatial steps, with 200 of them discretizing the section S_a.

Without loss of generality, one can assume a vanishing phase tuning δ in all sections but S_a, where $\delta \approx -0.8$ cm^{-1}, which allows to obtain a good agreement between the considered simple linear and more accurate nonlinear models for gain and index change functions. The absorption coefficients α in S_a and S_b are 2 cm^{-1} and 0 cm^{-1}, respectively. The attenuation $\eta = 0.8$ within S_g implies $\langle\alpha\rangle_g \approx 7.438$ m^{-1}.
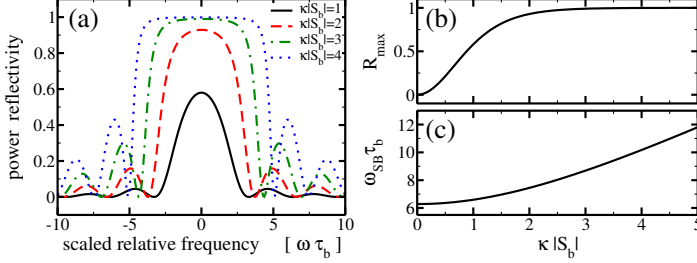

Figure 2: Reflectivity spectra of the BG for several values of $\kappa|S_b|$ (a). The dependence of the peak reflectivity (b) and stop-band width (c) on $\kappa|S_b|$.

In what follows, the properties of the BG are investigated. Fig. 2(a) shows spectra of the intensity reflection for different values of $\kappa|S_b|$ and for vanishing α and δ within S_b and vanishing reflection r_L at $z = L$. The maximal field intensity reflection R_{max} (achieved for the relative frequency $\omega_{\mathrm{max}} = -\delta c_0/n_g$) and the stop band width ω_{SB} are uniquely determined by the scaled coupling $\kappa|S_b|$:

$$R_{\mathrm{max}} = \tanh^2(\kappa|S_b|), \qquad \omega_{\mathrm{SB}} = \frac{2}{\tau_b}\sqrt{\kappa^2|S_b|^2 + \pi^2},$$

(see Fig. 2(b) and (c)). In the considered case, for $|S_b| = 6$ mm and $R_{\mathrm{max}} = 0.7$, the coupling coefficient $\kappa \approx 2.017$ cm^{-1} and the stopband width (measured as a separation of the adjacent to the stop band local minima of the reflectivity spectrum) $\omega_{\mathrm{SB}}/2\pi \approx 36$ GHz.

The thermal tuning factor $c_T \approx \pi/(|S_a|\Delta_I)$ implies the experimentally observed mode jumps with a change of the injected current [15, 11]. The value $c_T = 1.366 \cdot 10^5$ A^{-1}m^{-1} used in this paper corresponds to an average spacing between the mode jumps of $\Delta_I \approx 23$ mA and is in a good agreement with a similar parameter used in [15].

The remaining parameters are defined only within the active section S_a: $\overline{g} = 10^4$ m^{-1}, $\overline{\gamma} = 62$ ps^{-1}, $\overline{\omega} = 0$, $\Gamma = 0.027$, $N_{\mathrm{tr}} = 1.4 \cdot 10^{24}$ m^{-3}, $g' = 1.2 \cdot 10^{-19}$ m^2, $\alpha_H = 1.8$, $A = 3.33 \cdot 10^8$ s^{-1}, $B = 1 \cdot 10^{-16}$ m^{3}s^{-1}, $C = 2 \cdot 10^{-42}$ m^{6}s^{-1}, $\sigma = 2.24 \cdot 10^{-13}$ m^2. A small contribution of the spontaneous emission $F_{sp}^{\pm}$ is neglected when analyzing the TW model, but is taken into account when performing numerical simulations. More details on the meaning of the parameters can be found in Refs. [10, 15].

3 Mode analysis

It is well known that an analysis of optical modes of the model equations (1–6) can provide a deep understanding of different dynamic effects in various multi-section semiconductor lasers and, particularly, in ECDL devices. In this section, the concept of instantaneous optical modes will be introduced, and their relations to the cw states and dependence on the model parameters will be discussed. More details about this approach and its possible applications for analysis of the laser devices can be found in Refs. [13, 12, 11].

3.1 Instantaneous optical modes

Instantaneous optical modes are sets of complex-valued objects $(\Theta(z), \Omega)$, which satisfy the spectral problem generated by the substitution of the expression

$$E(z, t) = \Theta(z) e^{i\Omega t}$$

into the field equations (1), (2), and (4). Both $\Theta(z)$ and Ω depend on the instantaneous value of carrier density $N(t) = \bar{N}$. The real and imaginary parts of the complex eigenvalue Ω of the spectral problem represent an optical frequency and damping of the mode, respectively. The vector-eigenfunction $\Theta(z)$ gives us the spatial profile of the longitudinal mode [12].

For the simple case, when α_0, δ_0 in S_b, κ in S_a, and $r_{g',l}$, $r_{l,g''}$, $r_{g',b}$, r_L are vanishing, the substitution of the expression for the field function into (1) and the resolution of the resulting system of ODEs implies the complex equation

$$\mathcal{G}(\bar{N}, \Omega)\mathcal{R}(\Omega) e^{-2i\Omega\tau_g} = \eta^{-1} e^{-i\varphi}, \tag{8}$$

where the active-section and BG response functions $\mathcal{G}$ and $\mathcal{R}$, respectively, are given by

$$\mathcal{G}(\bar{N}, \Omega) = \frac{\Theta^+(z_{a,g'}^+)}{\Theta^-(z_{a,g'}^+)} = -\frac{\left(r_0^* + r_{a,g'}^* e^{i2D_a(\bar{N},\Omega)}\right)}{\left(r_0^* r_{a,g'} + e^{i2D_a(\bar{N},\Omega)}\right)},$$

$$D_a(\bar{N}, \Omega) = \Omega\tau_a + \left[\frac{(i+\alpha_H)\Gamma g'\left(\bar{N}-N_{\text{tr}}\right)}{2} + \frac{\overline{g}}{2}\frac{(\Omega-\overline{\omega})}{\overline{\gamma}+i\left(\Omega-\overline{\omega}\right)} - i\frac{\alpha}{2} + \delta + c_T I\right]|S_a|,$$

$$\mathcal{R}(\Omega) = \frac{\Theta^-(z_{g'',b}^-)}{\Theta^+(z_{g'',b}^-)} = \frac{-i\kappa|S_b|}{i\Omega\tau_b + D_b(\Omega)\cot D_b(\Omega)},$$

$$D_b(\Omega) = \sqrt{\Omega^2\tau_b^2 - \kappa^2|S_b|^2}.$$

The complex nonlinear characteristic equation (8) has an infinite number of complex roots Ω, most of which are well damped and play no role in the dynamics of the laser device (for more details see Ref. [12]).
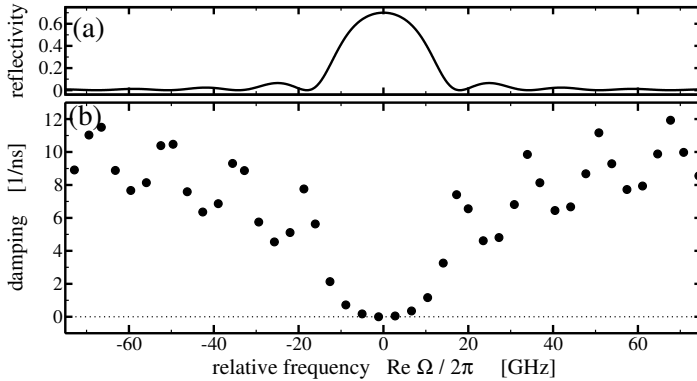

Figure 3: Field intensity reflectivity spectra of the BG (a) and complex frequencies Ω of the most important instantaneous modes (b) computed for $\bar{N} \approx 1.77 \cdot 10^{24}$ m^{-3}, which was obtained after the long transient integration of the TW model (1–6) for $I = 80$ mA.

A typical example showing most important mode frequencies Ω of the ECDL is given in Fig. 3(b). Note, that 5 modes located within the stop-band of the BG [see Fig. 3(a)] have rather small

damping, which does not exceed $1\,\mathrm{ns}^{-1}$. Thus, a strong influence of the side modes still can be expected, even though the ECDL operates at a cw state determined by one of these modes. Some possibilities for improving the mode selection will be discussed later in Section 5.

3.2 Stationary states

All stationary (continuous wave) states of the TW model (1–6) can be written as

$$\begin{pmatrix} E(z,t) \\ N(t) \end{pmatrix} = \begin{pmatrix} \Theta(z)e^{i\omega t} \\ \bar{N} \end{pmatrix}, \tag{9}$$

where $(\Theta(z), \omega)$ is an instantaneous optical mode computed at the mode *threshold* carrier density $\bar{N}$, which provides the *real*-valued mode frequency ω, i.e., determines the mode with no damping or amplification. Thus, in order to find all possible cw states we need to find all real pairs $(\bar{N}, \omega)$, which satisfy the characteristic equation (8). The method of definition of the cw states is similar to that frequently used in the analysis of the Lang-Kobayashi (LK) model for lasers with delayed optical feedback [6], where the corresponding cw states are well known as external cavity modes.

Once $\bar{N}$ and ω are known, one can easily reconstruct the spatial distribution of the optical fields (function $\Theta(z)$), which is a solution of the ODE system obtained after substitution of the field function from (9) into the TW problem (1), (2). The intensity P of the cw state emitted from the ECDL at the facet $z = 0$ can be found from the carrier rate equation (6):

$$P_{\mathsf{o}} = \frac{(1 - |r_0|^2)\sigma\frac{hc_0}{\lambda_0}\left(\frac{I}{q\sigma|S_a|} - A\bar{N} - B\bar{N}^2 - C\bar{N}^3\right)}{\left[\Gamma g'(\bar{N} - N_{\mathsf{tr}}) - \frac{\bar{g}(\omega - \overline{\omega})^2}{\bar{\gamma}^2 + (\omega - \overline{\omega})^2}\right]\frac{\left(e^{-\Im D_a} + |r_0|^2\right)\left(e^{\Im D_a} - 1\right)}{\Im D_a}}.$$

It is clear, that it only makes sense to discuss the cw states with positive intensity, i.e., the states with the threshold $\bar{N}$ satisfying the inequality $I > q\sigma|S_a|\left(A\bar{N} + B\bar{N}^2 + C\bar{N}^3\right)$.

The complex equation (8) for real frequency $\Omega = \omega$ and threshold density $\bar{N}$ is equivalent to the system of two real equations

$$\begin{aligned}
\eta &= \left|\mathcal{G}(\bar{N}, \omega)\mathcal{R}(\omega)\right|^{-1}, \\
\varphi &= 2\omega\tau_g - \arg\left[\mathcal{G}(\bar{N}, \omega)\mathcal{R}(\omega)\right] \mod 2\pi,
\end{aligned} \tag{10}$$

representing η and φ as the functions of two variables, $\bar{N}$ and ω. Thus, each pair $(\bar{N}, \omega)$ uniquely defines the values of η and φ, and, therefore, determine a cw state of the ECDL device with this pair of parameters. Those $(\bar{N}, \omega)$ giving $\eta = 0.8$ and $\varphi = 0$ (ECDL parameters defined in Subsection 2.3) are the roots of Eq. (10) and define the cw states of the considered ECDL.

A following geometric interpretation of Eqs. (10) suggests a relatively easy method for location of the roots $(\bar{N}, \omega)$ for any fixed parameters η and φ. Namely, each of the equations determines some curves in the $(\bar{N}, \omega)$ plane: see solid and dashed curves in Fig. 4. The intersections of different curves are the roots of Eq. (10) (bullets in the same figure).
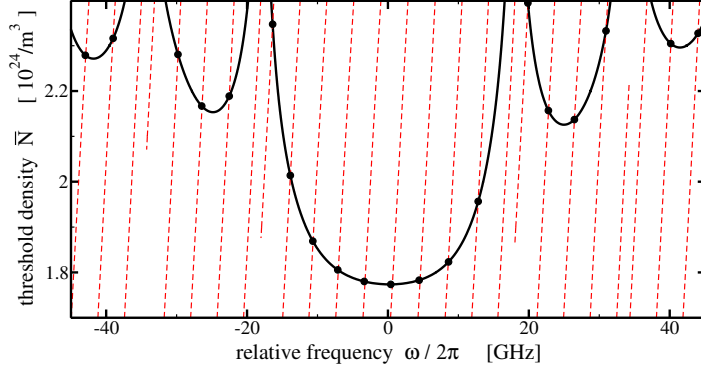
Figure 4: Representation of cw states in mode frequency ω - mode threshold $\bar{N}$ domain. Solid: cw states for fixed $\eta = 0.8$. Dashed: cw states for fixed $\varphi = 0$. Bullets: cw states for fixed φ and η. All other parameters as in Subsection 2.3.

The solid curves in Fig. 4, which are the contour lines of $\eta(\bar{N}, \omega)$, represent the roots of the considered system for $\eta = 0.8$ and arbitrary φ. The phase factor at each point of the curve can be easily determined by the second equation of (10). Thus, these curves are illustrating the continuation of all possible cw states (denoted by multiple bullets for $\varphi = 0$ in Fig. 4) when tuning the phase parameter φ. Tuning of φ leads to the shift of these states along the curves and the replacement of the next neighbor cw state on the curve with the periodicity $\varphi = 2\pi$.

Similarly, the dashed curves in Fig. 4 (the contour lines of $\varphi(\bar{N}, \omega)$ for $\varphi = 0$) correspond to cw states obtained by continuation of η. Sudden endings of these lines at certain values of ω are related to the zeroes of the function $\mathcal{R}(\omega)$ where factor η turns to infinity.

It is noteworthy, that the solid curves in Fig. 4 give a similar representation of the cw states as ellipses of external cavity modes in the LK model.

3.3   Multi-stability

The mode analysis and the location of the cw states discussed above do not provide any information about stability of these cw states. In general, a detailed investigation of the stability of the states can be performed by means of numerical bifurcation analysis [13]. In this paper, however, the stability of each cw state is identified by its ability to attract trajectories during numerical integration of the model equations.

The phase factor $\varphi = \varphi(\bar{N}, \omega)$ can be used for parameterization of the solid fixed-attenuation curves in Fig. 4. Thin solid curves in panels (a) and (b) of Fig. 5 show these parametric representations of $\omega = \omega(\varphi)$ and $\bar{N} = \bar{N}(\varphi)$, respectively. Due to the periodicity of factor φ, all these curves can be re-obtained after a 2π-shift along the abscissa axis. This periodicity implies the coexistence of multiple cw states for each fixed phase. For example, there are four states with $\bar{N} < 1.81 \cdot 10^{24}$ m^{-3} for $\varphi = 0$ (see number of solid lines at this phase in Fig. 5(b) and number of bullets for those threshold densities in Fig. 4).

Finally, the numerical integration of the TW model (1–6) over some long time interval with stepwise increasing (large red bullets in Fig. 5) or decreasing (small blue bullets in the same figure) phase factor φ was performed. At the end of each sub-interval where φ has been kept constant the main characteristics (minimal, maximal and mean intensity of the emission, mean carrier density, main lasing frequency, etc.) of the dynamic state were estimated. In order to identify sta-
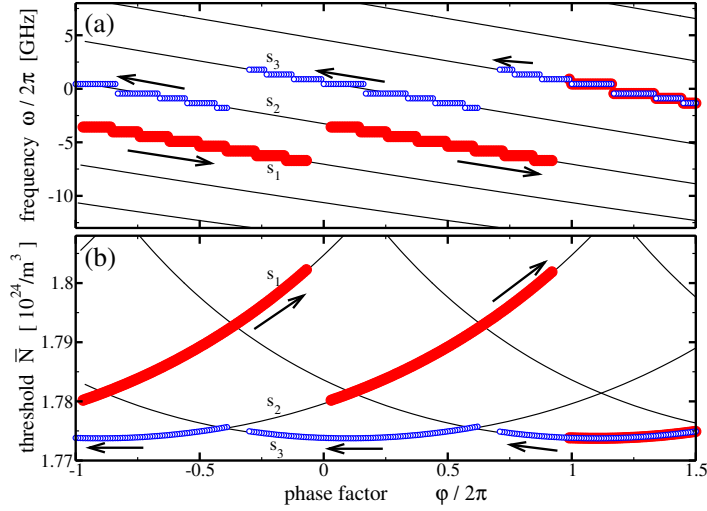
8

Figure 5: Frequencies ω (a) and thresholds $\bar{N}$ (b) of cw states as functions of phase φ for the injected current of 60 mA. Thin solid curves: cw states, i.e. the roots $(\bar{N}, \omega)$ of Eq. (10) for fixed $\eta = 0.8$. Large full red (small empty blue) bullets: stable states obtained by numerical integration of the TW model with step-wise increased (decreased) phase φ indicated also by the arrows. Other parameters as in Fig. 4.

ble cw emission, the side-mode suppression ratio μ_1 in the optical spectra (Fourier-transformed complex optical field $E^-(0, t)$ at the left facet of the ECDL) and the relative deviation

$$\mu_2 = \frac{\max_t P_o - \min_t P_o}{\max_t P_o + \min_t P_o}, \tag{11}$$

of the emitted field intensity $P_o(t)$ were determined. The observed stable states with $\mu_1 > 20\,\text{dB}$ and $\mu_2 < 0.02$ are indicated by red and blue bullets in Fig. 5. The bullets in panels (a) and (b) of this figure show the frequency ω of the main peak of the simulated optical spectra and the time-average of the computed carrier density, respectively.

It is noteworthy, that except for the tiny regions close to the observed transitions between the different states, the simulations show a stable cw emission. For decreased φ, the cw state is defined by the maximal gain (minimal threshold) mode. Once the threshold $\bar{N}$ of the adjacent mode approaches the threshold of the operating mode (close to $\varphi/2\pi = -0.35$ or 0.65), the switching to this side mode takes place. For increased φ, the situation is different. In most cases, the operating cw state is different from the maximal gain mode. Just before the state switches (at phases $\varphi/2\pi \approx 0$ or 1) the operating cw state is defined by the mode with the fourth smallest threshold. Moreover, the state transitions after the loss of stability in this case lead to different cw states. This is a manifestation of the multi-stability in the ECDL devices and is in a good agreement with the study of Ref. [9], where the stability of the stationary states in the LK model with a large delay was investigated.

Three different stable cw states were found for $\varphi/2\pi = -0.2$. The thresholds and the frequencies of these states, denoted as s_i, $i = 1, 2, 3$, are shown in Fig. 5, whereas the optical spectra and the emitted power of the field at both sides of the ECDL are represented in Fig. 6. It is not very surprising, that the smallest-threshold state s_3 has a largest emission at the active-section side of the ECDL (see Fig. 6(c)). Comparing to the other states, a smaller part of the injected current in this case is used to keep the carrier density at threshold, whereas the remaining larger part implies the larger emission. Probably, a bit unexpected is the large emission at the BG side shown by the largest-threshold state s_1 (see Fig. 6(d)). The wavelength of the state s_1, however, is more dislocated from the middle of the stop-band. Thus, the cw state s_1 gets a smaller
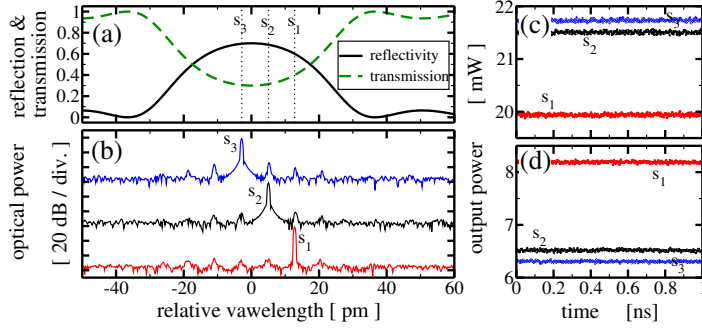
9

Figure 6: Simulated reflectivity and transmission spectra of the BG (a), optical spectra (b) and the emitted field power at the active-section (c) and BG (d) sides of the ECDL of three different stable cw states for $\varphi/2\pi = -0.2$. Other parameters as in Fig. 5.

reflection from the BG (what increases the mode threshold), but also has a larger transmission through the grating, which results in larger emission of the field (see Fig. 6(a,b)).

4   Experiments vs. numerical simulations

To validate the simulation results a micro-integrated ECDL with system parameters given in Subsection 2.3 was investigated in detail experimentally. The laser output emitted at the left facet of the laser chip (see. Fig. 1) was split to record the optical power and optical frequency vs. injection current simultaneously. For the measurements a laser diode controller ILX Lightwave LDC-3724C was used to drive the laser diode and to stabilize the temperature of the BG. Thermal stabilization of the micro-optical bench was provided by an ILX Lightwave LDT-5525C temperature controller. Optical power and optical frequency where measured with a powermeter (Coherent Inc. Fieldmaster with detector type LM-2 VIS) and a wavemeter (HighFinesse WS7), respectively.
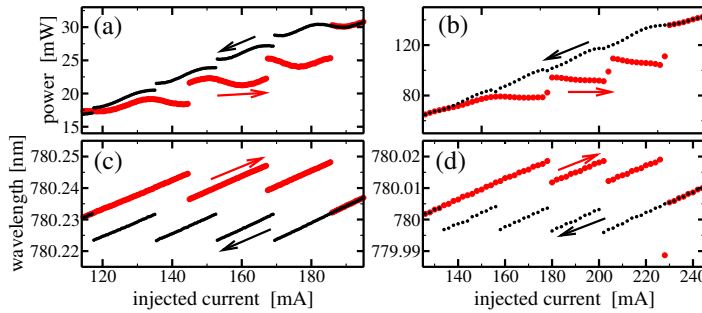

Figure 7: The mean output power at the left facet of the ECDL (a,b) and the dominant lasing wavelengths (c,d), as functions of the increased (red) or decreased (black) injected current in experiments (left) and simulations (right). In simulations, $R_{\max} = 0.5$, whereas all other parameters are as in Subsection 2.3.

A comparison of the measurements and simulations is performed in Fig. 7. Panels (a) and (c) of this figure represent typical experimentally observed state-exchange behavior in ECDL devices for increased and decreased injection currents induced by thermal detuning [11, 15]. One can see that the ECDL has multiple stable states, which can be accessed by changing the direction of the current sweep. The wavelengths of two different lasing states for $I \approx 125$ and $150\,\mathrm{mA}$ are separated by, approximately, $8.63\,\mathrm{pm}$, which corresponds to the separation of

10

the neighboring optical modes within the stop-band of the BG. The two times larger wavelength separation for $I \approx 140$ and between 155 and 186 mA indicates a possible coexistence of the third stable state, which could be accessed by a change of the direction of the current sweep just after each jump of the states.

The similar simulated state-jumping behavior is represented in panels (b) and (d) of the same figure. In order to obtain the good agreement between measurement and simulation, the maximum reflectivity of the BG has to been changed from the intended value $R_{\mathrm{max}} = 0.7$ to $R_{\mathrm{max}} = 0.5$ by a corresponding adaptation of the coupling coefficient κ. The reasons for this adjustment could be, for example, the divergence of the beam within the BG and an imperfect alignment of the BG with respect to the optical axis of the ECDL.

It is noteworthy, that the states observed during the down-sweeping of the injection current have larger intensities, as compared to the up-sweeping case. The wavelengths of these states are located close to the center of the BG stop-band, which in our simulations is at 780 nm. Small differences of the emitted field intensities before and after mode jumps in this case can be well explained by the similar emission power of the states s_3 and s_2, see Fig. 6(c) and discussion of Subsection 3.3. On contrary, the state jumps for up-swept injection correspond to detuning induced transitions between states s_1 and s_2 or s_1 and s_3 (see Figs. 5 and 6), what explains the large step-like increase of the emission intensity at each state transition.

5 Discussion

As it was mentioned above, the dynamics of the ECDL device is determined by several modes in many cases. In order to achieve a controllable stable lasing on a single mode, one needs to improve the mode selection, which, particularly, can be achieved by a reduction of the number of the main modes almost equally supported by the BG.

First of all, we consider the device with the BG peak reflectivity $R_{\mathrm{max}} = 0.7$. A detailed analysis of this ECDL device for increased and decreased injection current over larger injection range is presented in Fig. 8. The problem of frequently occurring multi-mode non-stationary states is well illustrated by panels (a) and (c) of this figure. Hatched regions in panel (a) indicate the existence of the non-stationary states with relative deviation factor $\mu_2 > 0.02$. In panel (c), small black and red dots showing the positions of side peaks with $\mu_1 < 20$ dB in optical spectra coincide with the wavelengths of the semi-analytically computed modes (thin grey-dotted lines). Thus, the dynamic states in these regions are determined by a beating between similarly damped longitudinal modes located within the stop-band of the BG. It is noteworthy, that for larger injection currents, $I > 150$ mA, up to five different modes can significantly contribute to the dynamic states (see multiple large and small bullets in Fig. 8(c) at these injection currents). At the same time, for smaller injection currents, $I < 100$ mA, only two or three modes can be excited, implying a more stable stationary operation of the device.

Increasing the injection current allows the achievement of stationary and non-stationary states with an (averaged) carrier density, that is significantly exceeding the density $\bar{N}$ of the minimal threshold mode (compare red and black curves in Fig. 8(b)). Typical increased injection-induced transitions between the states are characterized by the jumps to the shorter lasing wavelength
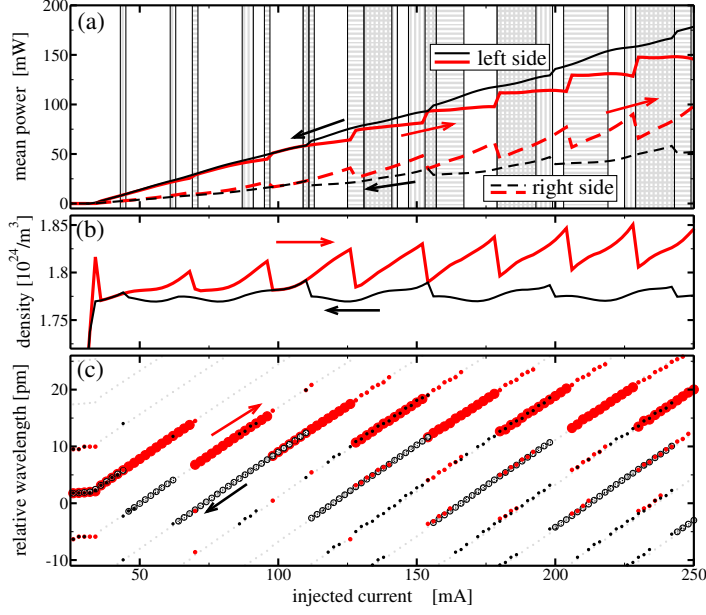
11

Figure 8: Mean output power at the left (solid) and right (dashed) sides of the ECDL (a), mean carrier density in S_a (b), and the lasing wavelengths (c) as functions of the increased (red) or decreased (black) injected current. All parameters are as in Subsection 2.3. Horizontally and vertically hatched areas in (a) indicate non-stationary regimes for increased or decreased currents, respectively. Big bullets and small dots in (c) represent the main optical mode and the side modes suppressed by less than 20 dB, respectively. Thin dashed grey lines in the same panel show positions of all longitudinal modes.

located closer to the central wavelength of the BG [red bullets in panel (c)], sudden reduction of the mean carrier density [panel (b)] and increase (decrease) of the (mean) emission intensity at the left (right) output port of the ECDL [panel (a)]. The lasing wavelength and emission intensities before and after the transitions are similar to those of the states s_1 and s_2 discussed in Subsection 3.3 and shown in Fig. 6. A corresponding transition from s_1 to s_2 was also shown in Fig. 5 at the phase $\varphi \approx 0$. The jumps of the carrier density and emission intensities for decreased injection current are less pronounced, since the dominant mode wavelengths are closer to the middle of the stop-band and their thresholds are rather similar.
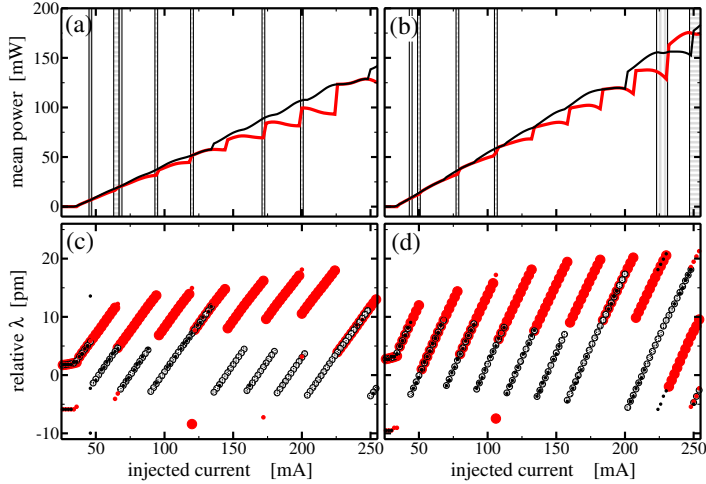

Figure 9: Mean left facet output power (top) and the lasing wavelengths (bottom) as functions of the increased (red) or decreased (black) injected current. Left: peak reflectivity $R_{\max} = 0.4$, air gap length $|S_{g''}| = 27$ mm. Right: $R_{\max} = 0.7$, $|S_{g''}| = 13$ mm. All other parameters are as in Subsection 2.3.

In what follows, we have repeated simulations of Fig. 8 using smaller κ and, therefore smaller reflectivity of the BG, $R_{\max} = 0.4$. As it can be seen from Fig. 9 (a) and (c), the reduction of κ

implies a reduction of the emission intensity at the left side of the ECDL, and, which is rather important, stabilizes the laser operation between the mode transitions. The gratings with large $\kappa|S_b| \geq 2$ have a flat stop-band [see Fig. 2(a)], which can equally support multiple modes (once they are located within such a stop-band). Thus, even though the choice of a smaller $\kappa|S_b| \approx 0.75$ [see Fig. 2(b)] reduces the overall reflectivity of the grating and implies an unwanted increase of the lasing threshold as well as decrease of the emission intensity, it helps to improve the side mode suppression.

Another way to achieve effective control of the modes is provided by a reduction of the air gap length, i.e., an increase of the mode separation and, therefore, the reduction of the number of modes supported by the BG. Panels (b) and (d) of Fig. 9 give an illustration of the simulated dynamics in the shortened ECDL with $|S_{g''}| = 13$ mm (compare it to $|S_{g''}| = 27$ mm used in the previous examples). It is noteworthy, that the stabilization of the ECDL in this case is achieved without the reduction of the emission power.
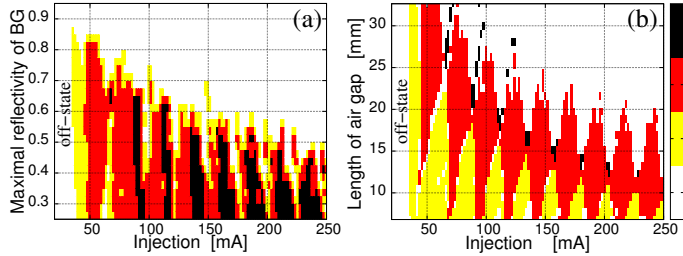

Figure 10: Number of stable cw states in ECDL devices for different values of injection current and tuned κ in the BG but fixed length $|S_g|$ (a) and tuned length $|S_g|$ but fixed κ in the BG (b). All parameters are as in Subsection 2.3.

A set of simulations of the ECDL devices with varying $R_{\max}$ and $|S_g|$ for different values of the injected current are summarized in panels (a) and (b) of Fig. 10. Here we show the number of stable coexisting cw states in different parameter domains in the absence of non-stationary attractors. White areas in these diagrams show the regimes were the ECDL is below threshold or posses at least one stable non-stationary regime. Yellow, red, and black colors indicate the parameters where a single, two or three different stable cw states could be observed. To access numerically each of these states, we have applied 10 ns long optical pulse injections with the optical frequencies determined by each of six modes located within the stop-band of the BG (see Fig. 3). The presence of the stable cw state was decided after 100 ns transients using the spectral and temporal criteria $\mu_1 > 20$ dB, $\mu_2 < 0.02$, as discussed in Section 3. Note also, that horizontal sections of diagram (a) at $R_{\max} = 0.4$ and of diagram (b) at $|S_g| = 16$ mm correspond to two situations considered in Fig. 9.

The white color regions at the upper right part of these diagrams confirm the occurrence of the mode beating solutions for high injection current and high $R_{\max}$ or long $|S_g|$. Thus, in order to manufacture devices with suppressed mode-beating dynamics within a large injected current range, one should use a moderate peak reflectivity of the BG and / or reduce the air gap length. The reduction of the air gap also implies a broadening of the injected current regions where the only lasing state is a continuous wave state: see yellow color regions at the lower part of Fig. 10(b).

13

Acknowledgments

References

[1] D. N. Aguilera *et al.*, "STE-QUEST-test of the universality of free fall using cold atom interferometry," Class. Quantum Grav., vol. 31, p. 115010, 2014.

[2] B. J. Bloom, T. L. Nicholson, J. R. Williams, S. L. Campbell, M. Bishof, X. Zhang, W. Zhang, S. L. Bromley, and J. Ye, "An optical lattice clock with accuracy and stability at the 10^{18} level," *Nature*, vol. 506, pp. 71–75, 2014.

[3] T. Sodnik, B. Furch, and H. Lutz, "Optical Intersatellite Communication," *IEEE J. Select. Top. Quant. Electron.*, vol. 16, pp. 1051–1057, 2010.

[4] E. Luvsandamdin, C. Kürbis, M. Schiemangk, A. Sahm, A. Wicht, A. Peters, G. Erbert, and G. Tränkle, "Micro-integrated extended cavity diode lasers for precision potassium spectroscopy in space," *Opt. Express*, vol. 22, pp. 7790–7798, 2014.

[5] B. Krauskopf and D.Lenstra, Eds., *Fundamental issues of nonlinear laser dynamics*. AIP Conf. Proc., vol. 548, 2000.

[6] R. Lang, and K. Kobayashi, "External optical feedback effects on semiconductor injection laser properties," *IEEE J. Quantum Electron.*, vol. 16, pp. 347–355, 1980.

[7] D. Lenstra, G. Vemuri, and M. Yousefi, "Generalized optical feedback: Theory," in *Unlocking dynamical diversity: Optical feedback effects on semiconductor lasers*, D.M. Kane and K.A. Shore, Eds. John Wiley Sons, West Sussex, 2005, pp. 55–80.

[8] V.Z. Tronciu, H.-J. Wünsche, M. Wolfrum, and M. Radziunas "Semiconductor laser under resonant feedback from a Fabry-Perot resonator: Stability of continuous-wave operation," *Phys. Rev. E*, vol. 73, 046205, 2006.

[9] S. Yanchuk and M. Wolfrum, "A multiple timescale approach to the stability of external cavity modes in the Lang-Kobayashi system using the limit of large delay," *SIAM J. Appl. Dyn. Syst.*, vol. 9, pp. 519–535, 2010.

[10] U. Bandelow, M. Radziunas, J. Sieber, and M. Wolfrum, "Impact of gain dispersion on the spatio-temporal dynamics of multisection lasers," *IEEE J. Quantum Electron.*, vol. 37, pp. 183–188, 2001.

[11] M. Radziunas, K.-H. Hasler, B. Sumpf, Tran Quoc Tien, and H. Wenzel, "Mode transitions in DBR semiconductor lasers: Experiments, simulations and analysis," *J. Phys. B: At. Mol. Opt. Phys.*, vol. 44, p. 105401, 2011.

[12] M. Radziunas and H.-J. Wünsche, "Multisection lasers: longitudinal modes and their dynamics," in *Optoelectronic devices – advanced simulation and analysis*, J. Piprek, Ed. Springer Verlag, 2005, pp. 121–150.

[13] M. Radziunas, "Numerical bifurcation analysis of traveling wave model of multisection semiconductor lasers," *Physica D*, vol. 213, pp. 98–112, 2006.

[14] H. Wenzel, K. Häusler, G. Blume, J. Fricke, M. Spreemann, M. Zorn, and G. Erbert, "High-power 808 nm ridge-waveguide diode lasers with very small divergence, wavelength-stabilized by an external volume Bragg grating," *Optics Lett.*, vol. 34, pp. 1627–1629, 2009.

[15] M. Spreemann, M. Lichtner, M. Radziunas, U. Bandelow, and H. Wenzel, "Measurement and simulation of distributed-feedback tapered master-oscillators power-amplifiers," *IEEE J. Quantum Electron.*, vol. 45, pp. 609–616, 2009.